

Native defects in sol–gel derived CdS buffer layers for photovoltaic applications

S. R. Meher¹ · Deepak K. Kaushik² · A. Subrahmanyam²

Received: 12 September 2016 / Accepted: 21 December 2016 / Published online: 10 January 2017
© Springer Science+Business Media New York 2017

Abstract Nanocrystalline CdS thin films are prepared by sol–gel dip coating for potential application as buffer layers in chalcogenide solar cells. X-ray diffraction and Raman spectroscopy results reveal that the films crystallize in hexagonal wurtzite structure. Spherical nano-grains with good surface coverage is observed in the scanning electron micrographs. The band gap values at different post-annealing temperatures are estimated from the optical absorption data. The surface work function which determines the band alignment at the heterojunction interface is obtained through Kelvin probe measurement. The native defects in CdS which can act as the recombination centers in chalcogenide solar cells are analysed by low temperature photoluminescence spectroscopy. The films annealed at 573, 623 and 673 K exhibit near infra-red emissions corresponding to the mid-gap cadmium vacancies. These kind of deep level hole traps are minimal for the films annealed at 723 K. The presence of strong exciton emission also ensures good crystalline quality of these films. The effect of mid-gap CdS acceptor density on the CIGS/CdS device performance has been studied through numerical simulation.

1 Introduction

Thin film photovoltaics research and development in the last two decades is mostly dedicated to the chalcogenides:

CdTe and CuInGaSe(S) (CIGS). The record efficiency registered for these cells is 22.1% and 22.3% respectively [1]. Many pilot lines are set up across the globe for the industrial production of CdTe and CIGS based solar cells. The most common *n*-type buffer layer for these chalcogenide solar cells is cadmium sulphide (CdS) [2]. This is because, CdS results in an optimal conduction band offset of -0.1 to 0.4 eV with these *p*-type absorbers [3, 4]. One of the inherent drawbacks of these cells with CdS as buffer layer is their poor blue response; the reason being its narrow optical band gap (~ 2.4 eV) [5]. The blue response of these cells is generally improved by reducing the thickness of CdS buffer layer.

Another major characteristics of the chalcogenide solar cells is the current (J)–voltage (V) distortions (cross-over and red-kink) which affects the overall cell performance [6–8]. One of the major reasons for the distortions in the J–V curve is the photo-doping [9] of CdS buffer layer which is an electronically compensated semiconductor. In CdS, the sulphur vacancies (V_S) and the cadmium interstitials (Cd_i) act as shallow donors [10]. The sulphur interstitials (S_i) act as shallow acceptors whereas cadmium vacancies (V_{Cd}^{2-}) and sulphur antisite defects (S_{Cd}) form deep level acceptors [11, 12]. The cadmium vacancy forms two different kinds of acceptor states in CdS [13]. The negative univalent vacancy (V_{Cd}^-) is a shallow level acceptor lying close to the valence band (VB). The bivalent state (V_{Cd}^{2-}) lies in the mid-gap region [12] and acts as the dominant hole trapping defect. These mid-gap acceptors are responsible for the near infra-red (NIR) emissions (1.2–1.5 eV) in the photoluminescence (PL) spectra [14, 15]. Under dark conditions, the concentration of these deep level acceptors is comparable to that of the shallow donors. At room temperature (300 K), these deep acceptors are ionized and are occupied by the electrons.

✉ S. R. Meher
samirmeher@gmail.com

¹ Department of Physics, School of Advanced Sciences, VIT University, Vellore 632014, India

² Department of Physics, Indian Institute of Technology, Chennai 600036, India

Therefore, the effective doping is strongly reduced. But under illumination, these negatively charged ionised acceptors easily capture a hole and become neutral. As a result, the effective *n*-type doping in CdS increases significantly and the energy band diagram gets modified. This leads to J–V distortions of the solar cell under standard AM1.5 illumination. The effect of photo-doping of CdS on the device performance however, is debatable. The mid-gap acceptors in one hand act as the recombination centers leading to a reduction in the minority carrier lifetime. On the other hand, the drift field created in ZnO window layer increases the collection efficiency of the photogenerated electrons. However, the numerical simulation performed in the present investigation (Sect. 4.7) predicts that more concentration of deep level acceptors (V_{Cd}^{2-}) results in an overall degradation of the device efficiency. The concentration of these kind of hole traps in CdS is strongly dependent on the deposition conditions and post-annealing effects.

CdS thin films can be deposited by a variety of techniques like chemical bath deposition (CBD) [16], electro-deposition [17], spray pyrolysis [18], sol–gel [19], thermal evaporation [20], sputtering [21], laser ablation [22], etc. The most common and cost-effective technique used in the photovoltaics industry for the deposition of CdS buffer layers is CBD. The major advantage of CBD is that it provides good surface coverage which allows to deposit very thin CdS layers (<50 nm) to enhance the blue response of the device. But, the chalcogenide solar cells with CBD grown CdS buffer layers usually exhibit J–V distortions which as discussed above are related to the concentration of deep level acceptors, mainly V_{Cd} . A reduction in V_{Cd} is required for better device performance due to decrease in the series resistance and an increase in the fill factor (FF) [23]. The as-grown CBD samples contain large number of lattice defects which can act as the “non-radiative recombination centers”. The annealed samples exhibit defect related photoluminescence (PL) arising due to the cadmium vacancies and interstitials.

The objective of the present work is to investigate a growth technique for which this mid gap defect level corresponding to V_{Cd} acceptors is minimized. Therefore in the present investigation, CdS thin films were grown using sol–gel dip coating method where the film stoichiometry can be well maintained. Sol–gel has got distinct advantage from other deposition techniques due to the atomic scale mixing of the constituents, ease of operation and reduced cost [24]. The as-deposited films were annealed at different temperatures (573, 623, 673 and 723 K) for 1 h in air. The effect of annealing on the defect related PL emission is studied in detail; the PL spectra were recorded at different temperatures in the range 93–300 K. The influence of CdS deep level hole traps on the J–V characteristics of a

model CIGS/CdS cell is investigated through numerical simulation.

2 Experimental details

CdS thin films were prepared by sol–gel dip coating method. Cadmium acetate (CdAc) ($\text{Cd}(\text{CH}_3\text{COO})_2$) and thiourea ($\text{CH}_4\text{N}_2\text{S}$) were used as the cadmium and sulphur precursors respectively. The chlorine precursors were avoided to get rid of chlorine related deep level traps. 0.3 M solutions each of CdAc and thiourea (20 ml each) were separately prepared in the organic solvent 2-methoxyethanol. The thiourea solution was added dropwise to the CdAc solution with continuous stirring. A few drops of (~1 ml) monoethanolamine was added as the sol-stabilizer to the final solution. The solution was stirred continuously for 2 h to get a homogeneous and transparent solution. Then it was aged for 4 h until gelation started and the colour of the solution became pale yellow. The CdS films were deposited on to pre-cleaned soda-lime glass substrates by dip coating method using a commercial microprocessor controlled dip-coater (Apex, ADIP-SV3). One side of the glass substrate was masked with cellulose tape. The dipping and withdrawal speed was maintained at 2 cm/min with a wet time of 30 s. After coating each layer, the films were preheated at 523 K for 5 min in air so that the organic residuals get evaporated. The cycle was repeated 10 times to get uniform films of ~200 nm thickness. The thickness of the films were obtained from spectroscopic ellipsometry (Woollam, M2000VI). Finally, all the films were annealed at different temperatures: 573, 623, 673 and 723 K for 1 h in air.

The phase and crystallinity of CdS thin films were studied using Phillips X’Pert Pro X-ray diffractometer operated at 40 kV and 30 mA using Cu $K\alpha$ radiation ($\lambda=0.1542$ nm). The micro-Raman spectra were collected (Horiba Jobin–Yvon LabRAM) at room temperature (300 K) with 442 nm excitation wavelength (He–Cd laser, M/s. Kimmon Koha). The signal was collected for 90 s in the backscattering geometry and was guided to a Peltier cooled charge-coupled device (CCD) detector. The PL spectra were obtained from the same He–Cd laser excitation source (442 nm). Liquid nitrogen was used for low temperature measurements through the Linkam THMS 600 stage. The optical absorption spectra of the films in the wavelength range (300–2500 nm) were measured using a JASCO double beam UV–Vis–NIR spectrophotometer (Model: V-570). Scanning electron micrographs (SEM) were recorded using a field-emission scanning electron microscope (FE-SEM) FEI Quanta 200. The surface work function was obtained by measuring the contact potential difference (CPD) between the sample and the gold coated stainless steel electrode using an indigenously developed

Kelvin probe set up [25]. More details regarding the Kelvin probe measurement is provided in the Appendix.

3 Simulation details

The numerical simulation to study the J–V characteristics of the model CIGS/CdS photovoltaic device was performed with the well-known programme SCAPS (Solar Cell Capacitance Simulator, Version 3.1.02) [26, 27]. SCAPS estimates the steady state band diagram, the recombination profile and the carrier transport in 1-dimension using the Poisson’s equation and the continuity equations for electrons and holes. The vertical cross-section of the device structure proposed in the present investigation is shown in the inset of Fig. 10. The details of the basic input parameters for different layers are given in Table 1.

4 Results and discussion

4.1 X-ray diffraction

Figure 1 shows the X-ray diffraction (XRD) patterns (20°–40°) of CdS thin films air-annealed (for 1 h) at different temperatures (573, 623, 673, 723 K). The films annealed

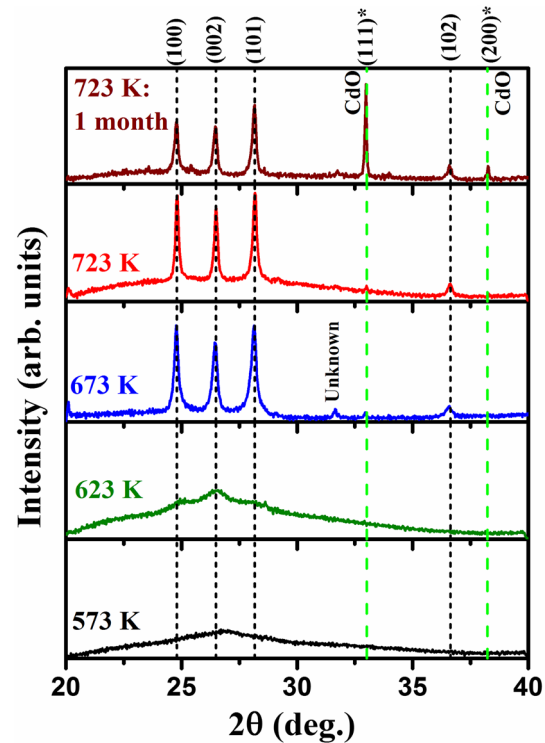


Fig. 1 (Colour online) XRD pattern for CdS films air-annealed at different temperatures

Table 1 Summary of SCAPS input parameters for model CIGS/CdS solar cell

Parameter	CIGS	CdS	<i>i</i> -ZnO	Al:ZnO
Thickness (μm)	2.5	0.08	0.05	0.2
Bandgap (eV)	1.2	2.48	3.3	3.3
Electron affinity (eV)	4.4	4.2	4.55	4.55
Dielectric permittivity (relative)	10	8.9	8.12	8.12
N_C (/cm ³)	1.91×10^{18}	2.52×10^{18}	4.1×10^{18}	4.1×10^{18}
N_V (/cm ³)	2.58×10^{18}	2.01×10^{18}	8.2×10^{18}	8.2×10^{18}
v_{th} (electrons, cm/s)	2.75×10^7	2.12×10^7	1.73×10^7	1.73×10^7
v_{th} (holes, cm/s)	2.12×10^7	1.18×10^7	1.03×10^7	1.03×10^7
Shallow N_A (/cm ³)	1×10^{16}	0	0	0
Shallow N_D (/cm ³)	0	1×10^{17}	1×10^{10}	1×10^{20}
μ_n (cm ² /V.s)	50	50	100	100
μ_h (cm ² /V.s)	30	20	20	20
A (cm ⁻¹ eV ^{1/2})	5×10^4	5×10^4	5×10^4	5×10^4
Defect type	<i>d</i>	<i>a</i>	<i>n</i>	<i>n</i>
Defect distribution	Gaussian	Gaussian	Single	Single
Total defect density (/cm ³)	10^{15}	Variable	10^{12}	10^{14}
σ_n (cm ²)	10^{-14}	10^{-16}	10^{-15}	10^{-15}
σ_h (cm ²)	10^{-16}	10^{-14}	10^{-15}	10^{-15}

N_C conduction band effective density of states, N_V valence band effective density of states, v_{th} thermal speed, N_A/N_D acceptor/donor density, μ_n/μ_h electron/hole mobility, A optical absorption constant, a acceptor, d donor, n neutral

Back contact work function: 5.4 eV, front contact: flat band conditions

Series resistance: $1 \Omega \text{ cm}^2$, shunt resistance: $10^4 \Omega \text{ cm}^2$

at 573 K shows amorphous nature with a broad hump $\sim 26^\circ$. The crystallization of the films starts at 623 K and it improves with increase in the annealing temperature. The films crystallize in hexagonal wurtzite structure with characteristic diffraction peaks corresponding to (100), (002), (101) and (102) planes [JCPDS 41-1049]. The hexagonal phase is stable for CdS at high temperatures and ambient pressure. For the films annealed at 673 and 723 K, a minute peak corresponding to (111) plane of cubic CdO appears at 33.04° [JCPDS 65-2908]. The formation of CdO on the surface of CdS has been reported by several authors [19, 28]. It is attributed to the conversion of unstable cubic CdS to CdO at higher temperatures in air atmosphere. The films annealed at 723 K and kept under ambient conditions for 1 month exhibit high intensity diffraction peaks corresponding to (111) and (200) planes of cubic CdO. These peaks disappear after re-annealing the samples in air at 723 K and the original XRD pattern corresponding to hexagonal CdS is regained. This indicates that CdO formation is due to the atmospheric moisture and is limited to a few monolayers (<10 nm). This oxide layer can be minimized by re-annealing the samples. A small peak at 31.7° is observed for the CdS films annealed at 673 K. Chu et al. [29] have also observed this peak for annealed CdS films and have attributed this to sodium containing impurities from the glass substrate. The average crystallite size for the films annealed at 673 and 723 K was calculated using Scherrer's semi-empirical formula,

$$D = \frac{0.9\lambda}{\beta \cos \theta} \quad (1)$$

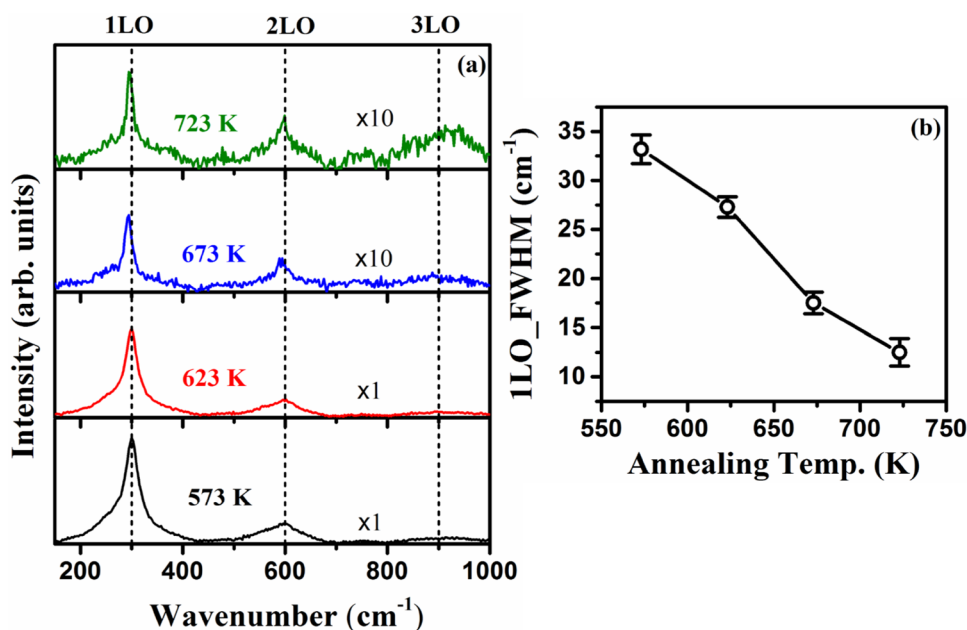
where, $\lambda=0.1542$ nm and $\beta=B-b$ (B being the observed FWHM and b is the instrument function

determined from the broadening of the monocrystalline silicon diffraction line). The average crystallite size along (002) plane was found to be 28 nm and 48 nm for the films annealed at 673 K and 723 K respectively. The lattice parameters c and a obtained for the CdS films annealed at 723 K are 0.6728 nm and 0.4143 nm respectively. These values match closely with the crystallographic data for hexagonal bulk CdS [30]. All further characterizations were performed for the freshly annealed samples.

4.2 Raman spectroscopy

The room temperature (300 K) Raman spectra for CdS films annealed at different temperatures are shown in Fig. 2a. All the films exhibit the characteristic vibrational modes corresponding to the hexagonal wurtzite structure [31]. The well resolved highest intensity peak at ~ 300 cm^{-1} is due to the first order scattering of the longitudinal optical (1LO) phonon modes. The second and third order LO modes are observed with reduced intensities at ~ 600 cm^{-1} and 900 cm^{-1} respectively. The small shift of the 1LO peak towards the lower wavenumber (compared to that of the bulk CdS) is attributed to the grain size effects [32]. No additional peak corresponding to the oxide phase is observed even at higher annealing temperatures. The peaks are fitted with standard Lorentzian function and the full width at half maximum (FWHM) of 1LO peak is shown as a function of annealing temperature in Fig. 2b. The FWHM is found to be decreasing with the annealing temperature which is a signature of better crystallinity in accordance with the XRD data. The shifting of the peak position and the decrease in the peak intensity for higher annealing

Fig. 2 (Colour online) (a) Raman spectra for CdS annealed at different temperatures. **b** Variation of FWHM corresponding to 1LO phonon scattering with annealing temperature



temperatures may be associated with the oxygen incorporation into the lattice which also appears as a small impurity peak corresponding to the cubic CdO in XRD.

4.3 Surface morphology

The scanning electron micrographs of the CdS films annealed at 673 and 723 K are shown in Fig. 3. Well defined randomly oriented grains are observed with good substrate coverage. The surface is crack free with a few nanometer sized pinholes especially for the films annealed at 723 K. This is due to the proper densification of the grains at higher annealing temperatures leaving behind some voids. The presence of pinholes are also common in CBD grown films. They are responsible for low shunt resistance by providing an alternate current path for the light generated current in thin film solar cells [33]. Therefore, a high resistance ZnO window layer is usually deposited over the CdS buffer layer to minimize the leakage current in CIGS or CdTe based devices. Moreover, the grain boundary scattering plays an important role in the carrier transport and effects the photovoltaic performance. The average grain size are found to be 50.8 nm and 83.3 nm for the films annealed at 673 K and 723 K respectively. Therefore, the CdS films annealed at 723 K are anticipated to have improved carrier transport properties. The grain size obtained from SEM follows the similar trend as that of the average crystallite size calculated from the XRD pattern.

4.4 Optical absorption studies

The optical band gap values of CdS thin films were determined from the optical absorption measurements following the well-known Tauc's plots (Fig. 4). CdS is reported to be a direct band gap semiconductor [34] and according to the

model for direct allowed transitions (under parabolic bands approximation), the band gap values can be obtained by extrapolating the linear part of $(\alpha h\nu)^2 \sim h\nu$ plot intercepting the energy axis. Here, α is the corresponding absorption coefficient which can be calculated from the film thickness and absorbance data. The band gap values are found to be slightly decreasing from 2.49 to 2.44 eV with increase in the annealing temperature (Fig. 4e). The small decrease in the band gap with an increase in the annealing temperature can be attributed to the relaxation of lattice strain and quantum confinement effect [19]. The non-linear tail absorption at lower energies may be associated with the absorption of long wavelength phonons [35]. The band gap values are in close agreement with that of single crystal CdS [36] within the measurement errors.

4.5 Photoluminescence studies

Photoluminescence (PL) is a powerful tool to analyse the defects in a semiconductor which take part in the radiative recombination processes. CdS is a compensated semiconductor containing large number of shallow and deep level defects. The nature and type of defects is strongly dependent on the deposition conditions and accordingly the PL emission varies. For room temperature (300 K) PL, the band edge emission lies around 2.4–2.5 eV [37, 38]. At lower measuring temperatures, the peak at ~2.54 eV is reported to be due to the donor bound excitons [39]. The broad peak around 550–700 nm (2.25–1.70 eV) has been identified in the literature to be due to the native defects such as Cd_i , V_{Cd} , S_i and V_S [14, 40]. As mentioned earlier, V_{Cd}^- lies near to the VB at ~0.1–0.2 eV and forms a Frenkel defect complex with Cd_i [14]. The bivalent cadmium vacancy ($\text{V}_{\text{Cd}}^{2-}$) lies in the mid-gap region at ~0.9–1.2 eV from the VB edge [12, 15, 41]. The antisites

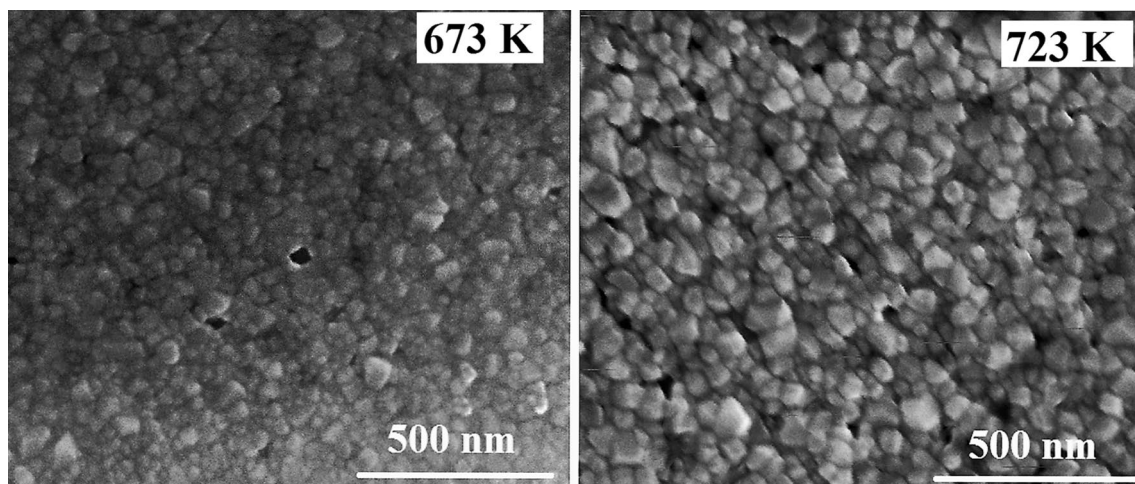


Fig. 3 SEM micrographs for CdS thin films annealed at 673 and 723 K

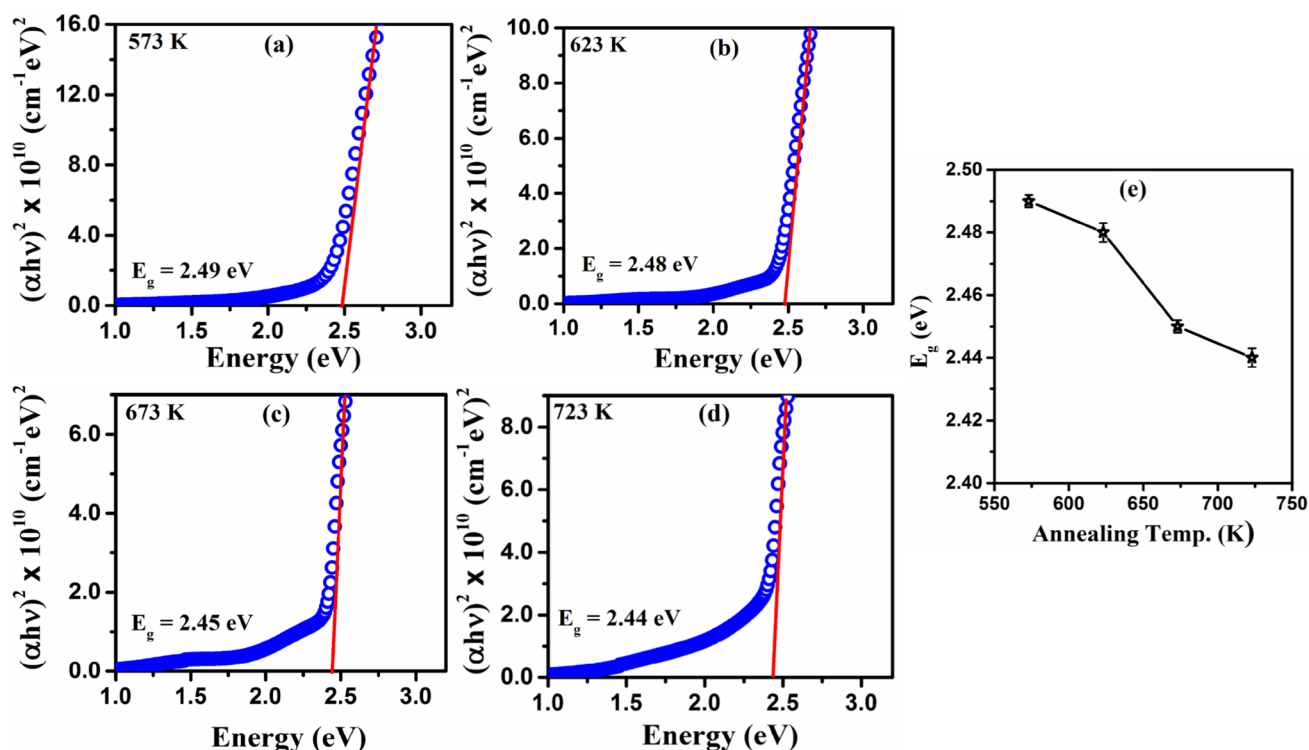


Fig. 4 (Colour online) (a–d) $(\alpha h\nu)^2$ vs. $h\nu$ plots for CdS films annealed at different temperatures showing the optical band gap (e) variation of band gap with annealing temperature

of sulphur (S_{Cd}) which are rarely reported in the literature also form deep level acceptors [12]. The sulphur interstitials form shallow acceptor levels and lie at ~ 0.11 – 0.15 eV above the VB [40, 42]. The cadmium interstitials act as the dominant shallow donors at ~ 0.1 – 0.2 eV below the conduction band (CB) edge [11, 40]. The bivalent sulphur vacancies lie at ~ 0.6 – 0.7 eV below the CB forming the relatively deeper donor states [11, 14]. All the above mentioned native defects are reported to take part in the radiative recombination processes and result in PL emissions. The green band (2.2–2.4 eV) in CdS PL spectra is usually associated with a transition between a shallow donor (Cd_i) and VB or a transition between a shallow acceptor (S_i) and CB [11]. A few groups suggest that the green band originates due to a transition between the sulphur vacancies and the VB [40]. The orange and yellow band (1.9–2.2 eV) is attributed mostly to the donor-acceptor-pair (DAP) recombination of ($Cd_i - V_{Cd}^-$) Frenkel defect complexes. The red band-I (1.7–1.9 eV) has been ascribed to the transitions from sulphur vacancy states to VB [40]. The red band-II (1.6–1.7 eV) is caused by the transitions of electrons trapped in surface states (mostly related to V_S) to the VB [14]. The NIR band (1.2–1.5 eV) is associated with the radiative transitions from the CB or Cd_i levels to mid-gap acceptors (V_{Cd}^{2-}). For the present study, the room temperature PL spectra of the sol–gel prepared CdS films

post-annealed at different temperatures are shown in Fig. 5. For further analysis, the spectra were converted to energy units by rescaling the signal values with the Jacobian transformations (hc/E^2). The resulting PL spectra with energy units were fitted and deconvoluted with Voigt profile fitting to analyse the type of radiative transitions.

CdS films annealed at 573 K (Fig. 5b) is mainly dominated by a broad defect peak in the red-infra-red region. At lower annealing temperatures, the surface defect states are abundant due to large number of crystallographic disorder. The surface defect states are mostly the sulphur vacancies. The peak at 1.65 eV corresponds to these defects. A broad peak at 1.70 eV can be due to the radiative transition between the bulk V_S and VB. At lower annealing temperatures, the cadmium atoms may not be properly placed into the lattice sites resulting in distortions, cadmium and sulphur vacancies and interstitials. The broad low intensity green band at 2.32 eV arises due to the transition between Cd_i and VB. The NIR peak at 1.39 eV originates due to the transition from CB or Cd_i to V_{Cd}^{2-} states. The low PL intensity is due to the presence of large number of non-radiative channels present at lower annealing temperatures.

For 623 K annealed films (Fig. 5c), the PL spectra shows some additional features in the high energy side. The small intensity peak at 2.38 eV is either due to the cadmium interstitials or due to the sulphur interstitials (Cd_i or S_i).

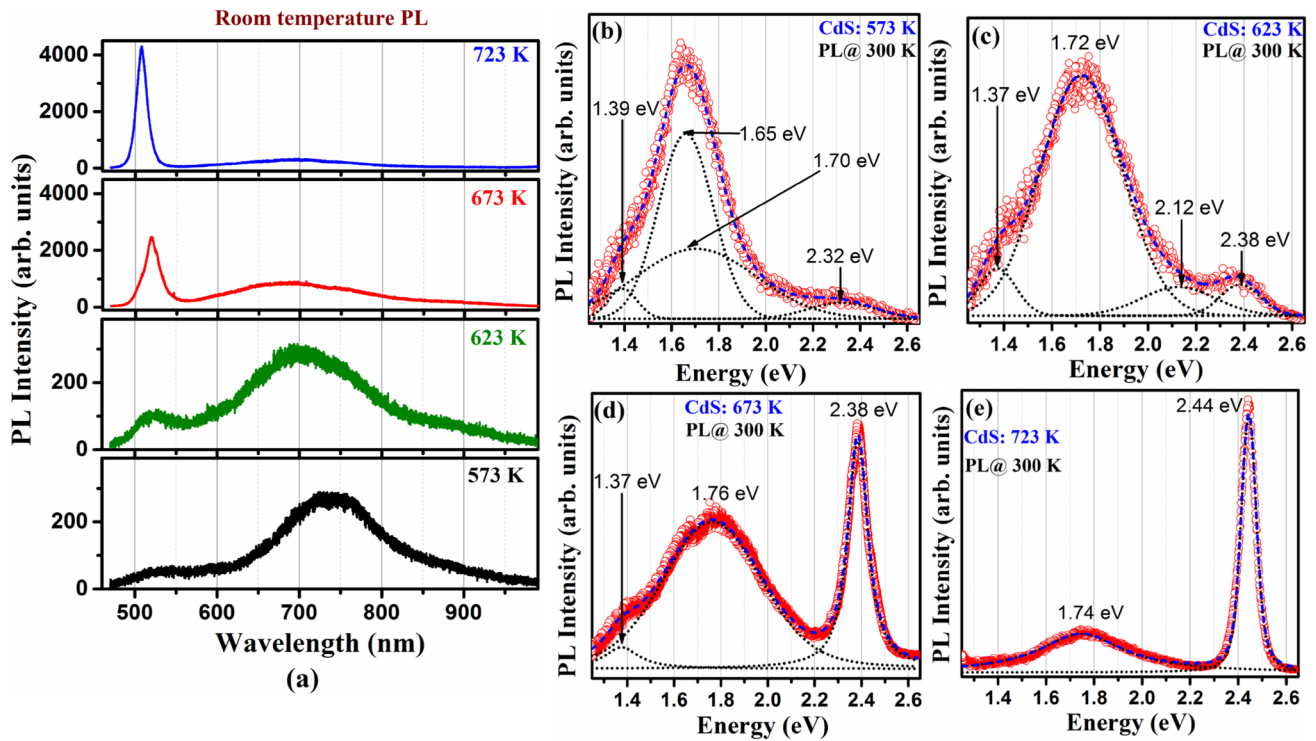


Fig. 5 (Colour online) (a) Room temperature PL spectra for CdS films annealed at different temperatures (b–e) Fitted PL spectra showing radiative transitions at different annealing temperatures

The orange band deconvoluted at 2.12 eV is attributed to the DAP recombination of $(Cd_i - V_{Cd}^-)$ defect complexes. The peak for the red-band corresponding to sulphur vacancies appears at 1.72 eV. The bivalent V_{Cd}^{2-} which form the mid-gap acceptors give rise to the PL emission in the NIR region at 1.37 eV. The crystallization of the films starts at 623 K which helps in reducing the non-radiative recombination centers and an increase in the PL intensity.

With further increase in the annealing temperature (673 K), the crystallization in the CdS films improves and the surface defects are minimized (Fig. 5d). The lattice strain is released and there is an increase in the grain size. Therefore, the red band-I which is due to the surface defects is no longer present in the PL spectrum. The red band-II which is due to the bulk sulphur defects is visible. The transition from bulk V_S to VB results in the PL emission at 1.76 eV. But, still a small contribution from mid-gap acceptors (V_{Cd}^{2-}) is visible with a broad NIR defect peak centered at 1.37 eV. The green emissions near the band edge is more sharp and intense compared to the films annealed at 573 and 623 K. As discussed before, the emission peak at 2.38 eV can be attributed either to Cd_i or S_i . Hence it can be inferred that for the sol–gel prepared CdS films, still higher annealing temperature is required for the interstitial Cd and S atoms to occupy the lattice sites to reduce the number of vacancies. However, the role of interstitial

oxygen in the green band cannot be ruled out. Gemain et al. [43] have observed the optical signature of interstitial oxygen at 2.35 eV. They have assumed that the interstitial oxygen atoms replace the interstitial sulphur atoms in case of post-growth oxygen treatment. The decrease in other non-radiative channels explains the increase in PL intensity.

The PL spectrum for CdS films annealed at 723 K (Fig. 5e) shows a narrow intense emission at 2.44 eV with a broad defect emission centered at 1.74 eV. The room temperature PL emission at 2.44 eV is due to the recombination of free excitons (X). At room temperature, the thermal energy is comparable to the reported exciton binding energy of single crystal CdS (~28 meV) [44]. These excitons are thermally dissociated only when the thermal energy exceeds the corresponding binding energy. The presence of strong and narrow exciton peak signifies the high crystalline quality of CdS samples annealed at 723 K. Many reports have suggested that CdS dissociates at higher annealing temperatures giving rise to cadmium interstitials and sulphur vacancies [14]. The dissociation of CdS causes the diffusion of Cd atoms into the underneath CIGS absorber layer which deteriorates the CIGS/CdS photovoltaic *p-n* junction [45]. But in the present study, the dissociation rate of CdS is reduced because of the atmospheric annealing of CdS thin films. It is well known that the Gibbs free energy of the reaction becomes more positive

as temperature increases and consequently the equilibrium constant for the reaction decreases [46]. The equilibrium constant (K) is related to the Gibbs free energy (ΔG_R) of the reaction as,

$$K = \exp\left(-\frac{\Delta G_R}{RT}\right) \quad (2)$$

where R is the gas constant and T is the absolute temperature. During the annealing of CdS films under atmospheric pressure (air ambience), the Gibbs free energy of the reaction ΔG_R is less positive. So, the reaction equilibrium constant K is high in this case (air annealing) and the reaction favours more towards product side. Consequently the decomposition is lesser as compared to the vacuum annealing. The same is also confirmed from the XRD pattern where the crystallinity is improved at higher annealing temperature of 723 K. Therefore, the sulphur vacancies arising due to the CdS dissociation are minimal and they contribute only to a low intensity defect peak at 1.74 eV. Some of the sulphur vacancies are also expected to be occupied by oxygen which acts as an isoelectronic impurity. The oxygen incorporation into the lattice results in a reduction in V_S [47]. However, no defect emission in the NIR region corresponding to mid-gap acceptors (V_{Cd}^{2-}) is observed. Therefore, it can be inferred that the photo-doping phenomenon is minimal for the films annealed at 723 K and hence are ideal candidates to be used as buffer layers in chalcogenide solar cells. Moreover, the green PL emission due to cadmium interstitials or oxygen impurities may be buried in the background of strong exciton emissions. In order to verify this and to look for other exciton related emissions, low temperature PL measurements were carried out for the samples annealed at 723 K. Based on the above discussion, the tentative energy level diagram for the CdS thin films prepared by sol-gel dip coating is proposed in Fig. 6.

The temperature dependent PL spectra (93–300 K) for CdS films annealed at 723 K is shown in Fig. 7a. The PL signal is seen to be quenched at higher measuring temperatures because of the availability of more number of non-radiative recombination channels. These non-radiative channels are in competition with the radiative transitions at higher measuring temperatures. At lower measuring temperatures, the high energy narrow peak becomes intense and asymmetric, indicating the presence of more than one kind of emissions. At lower temperatures, the narrowing down of exciton peaks is because of the reduction of impurity scattering. The fitting of high energy asymmetric peak at 93 K is shown in Fig. 7b. The highest intensity peak at 2.53 eV corresponds to the annihilation of free excitons. The neighbouring peak at 2.50 eV is ascribed to neutral-donor bound exciton (D^0-X) emission reported to be arising due to oxygen impurities [43]. The cadmium and oxygen interstitials contribute to the small but broad defect

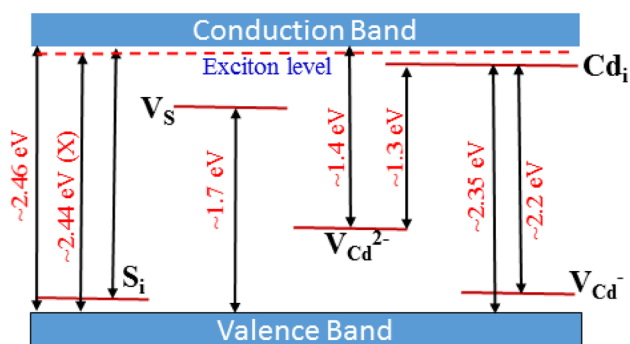


Fig. 6 (Colour online) Schematic of the proposed energy band diagram for CdS thin films prepared by sol-gel dip coating

emission at 2.44 eV. The temperature dependence for energy band gap of the CdS thin films annealed at 723 K can be obtained by adding the exciton binding energy (28 meV) to the free exciton emission energy. The energy corresponding to the free exciton emission as well as the band gap values as a function of temperature are shown in Fig. 7c. The band gap values at different temperatures $E_g(T)$ are fitted with Varshni's relation given as [48]:

$$E_g(T) = E_g(0) - \frac{\alpha T^2}{\beta + T} \quad (3)$$

Here, α and β are Varshni's constant. The best fitted value for α and β is $(1.52 \pm 0.7) \times 10^{-3}$ eV/K and 1099 ± 666 K respectively. The parameter β is believed to be related to the Debye temperature of the material. The band gap at 0 K ($E_g(0)$) is estimated to be 2.565 ± 0.002 eV. Further, the intensity of exciton PL emission is plotted as a function of temperature in Fig. 7d. The PL intensity is observed to be decreasing with increase of temperature.

The defect PL emission at 93 K is shown in Fig. 8a. The deconvoluted peaks at 1.95 and 1.72 eV corresponds to DAP ($Cd_i - V_{Cd}^-$) recombination and V_S -VB transitions respectively. The low temperature PL emission at 93 K for the CdS thin films annealed at 673 K is shown in Fig. 8b, c. A small but narrow peak at 2.52 eV is believed to be due to the exciton emission. The two broader peaks in the high energy side at 2.45 eV and 2.37 eV is due to Cd_i and S_i interstitials respectively. The other defect peaks at 1.91 eV, 1.79 eV, 1.65 eV and 1.41 eV is attributed to DAP recombination, V_S (bulk and surface) and V_{Cd}^{2-} respectively.

4.6 Surface work function

The conduction band offset (cliff or spike type) between the absorber and buffer layer plays an important role in solar cell device performance. A cliff like band offset limits the open circuit voltage due to increased probability of interface recombination. A larger spike in the conduction band

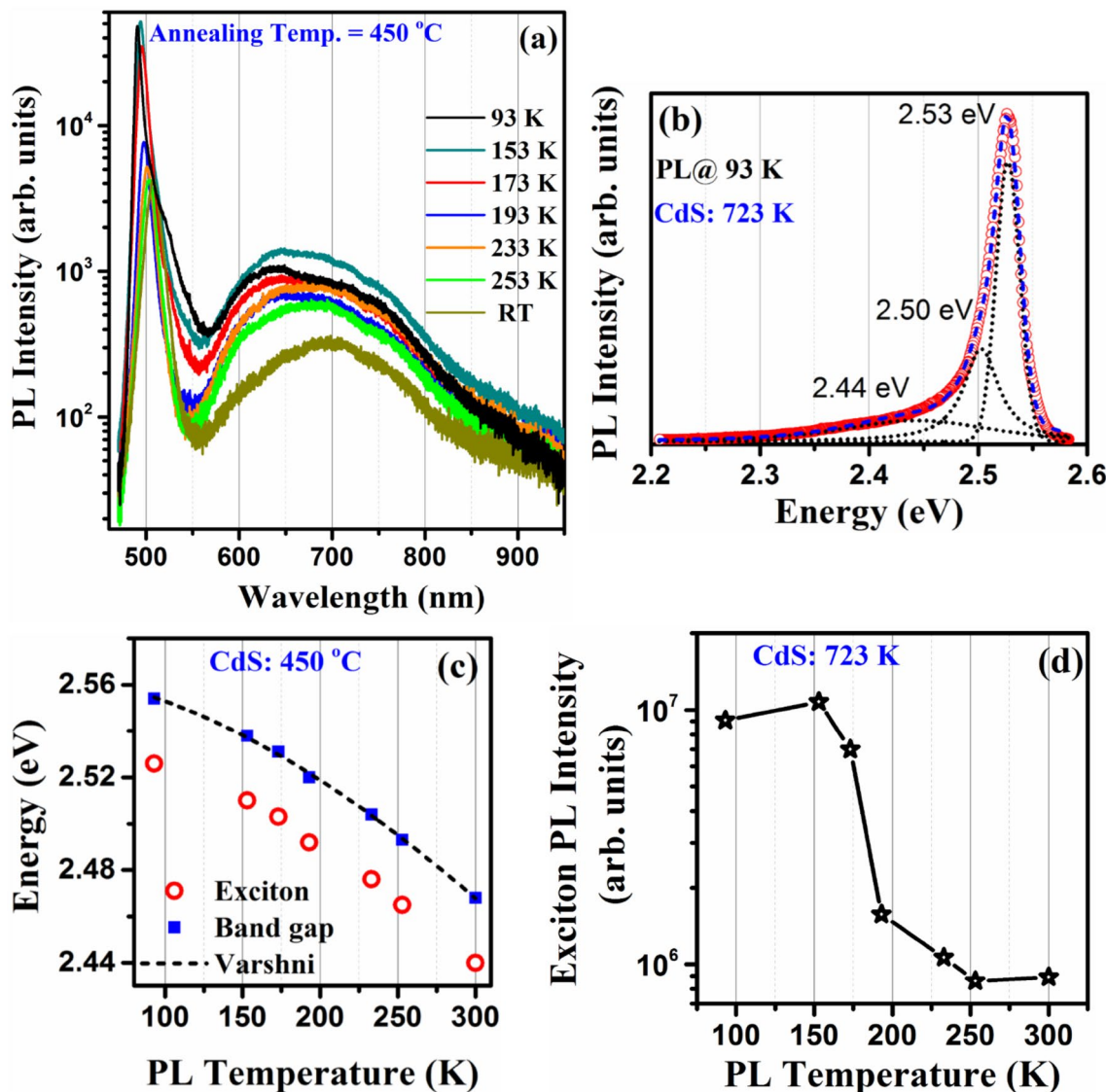


Fig. 7 (Colour online) **(a)** Low temperature (93 K–RT) PL spectra for CdS thin films annealed at 723 K. **(b)** Fitted PL spectrum (at 93 K) in the high energy side showing the exciton related emissions and broad defect emission. **(c)** Band gap variation as a function of measur-

ing temperature (*dashed black line* is the fitting for Varshni’s equation). **(d)** Exciton emission intensity as a function of PL measuring temperature for CdS films annealed at 723 K

prevents the flow of minority carriers and reduces the conversion efficiency. Therefore an optimum spike like band offset (0.1–0.4 eV) is required for better efficiency. The band alignment at the interface is decided by the surface work functions or electron affinities of the absorber and buffer layer. Kelvin probe measurement is a non-destructive technique to evaluate the surface work function of metals and semiconductors. It measures the Fermi levels of the sample with respect to the reference electrode and the corresponding potential difference is known as contact potential difference (CPD) [25]. This CPD is directly proportional to the work function of the sample under consideration. The CPD values for the CdS samples annealed at

different temperatures are shown in Fig. 9 for a scan area of 1.0×0.6 mm². The CPD for all the films are found to be in the range 55–65 mV. The corresponding surface work function for CdS films annealed at different temperatures lie in the range 4.70–4.71 eV.

4.7 Numerical simulation

In order to evaluate the effect of CdS mid-gap acceptors on the photovoltaic device performance, a model CIGS/CdS solar cell was simulated. The proposed device structure is shown in the inset of Fig. 10. The basic input parameters were chosen from the literature and are given in Table 1.

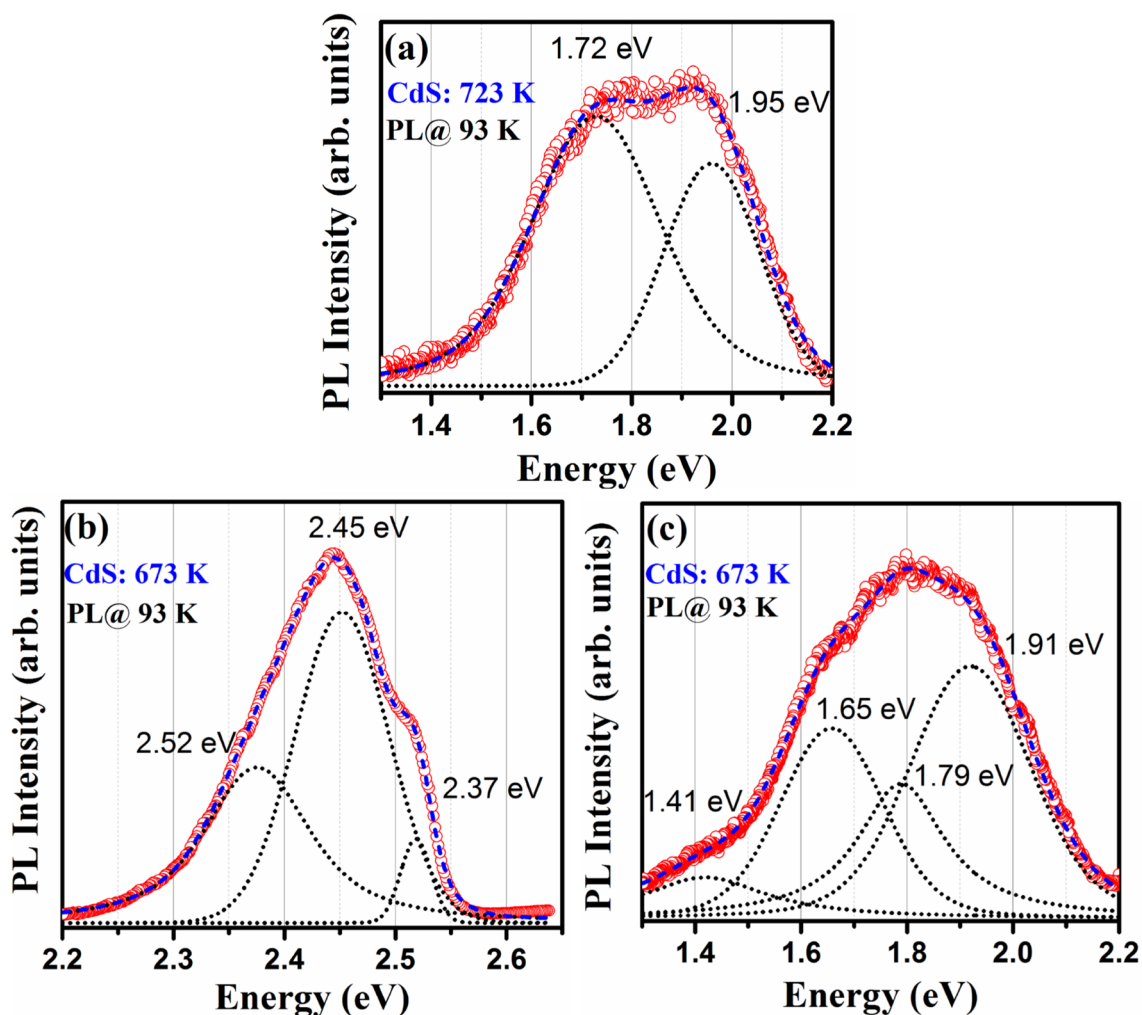


Fig. 8 (Colour online) (a) Defect related PL emission collected at 93 K in the lower energy side for CdS films annealed at 723 K. **b, c** Deconvoluted PL spectra (at 93 K) for CdS films annealed at 673 K

The mid-gap acceptors (V_{Cd}^{2-}) were assumed to be at 1 eV above the VB edge. The distribution was taken to be Gaussian and the total defect density was varied from 10^{15} to 10^{18} cm^{-3} . The carrier capture cross-section was assumed to be asymmetric because, it is affected by the Coulombic interaction for charged defects. For Coulombic attraction the carrier capture cross-section (10^{-14} cm^2) was taken to be two orders of magnitude higher than that of Coulombic repulsion (10^{-16} cm^2). The solar cell efficiency as a function of CdS mid-gap acceptor density is shown in Fig. 10. The efficiency is affected severely once the defect density exceeds 10^{16} cm^{-3} . The simulated J–V characteristics under different illumination conditions for CdS mid-gap acceptor density of 10^{17} cm^{-3} is shown in Fig. 11a. The J–V characteristic shows typical cross-over between the dark and AM1.5 illuminations. This kind of J–V cross-over is common in CIGS based solar cell and is attributed to the photo-doping of CdS buffer layer [6]. The energy band

diagram for the model solar cell is shown in the inset. It can be seen that for low energy photons (600 nm) or in dark, electron–hole pairs are not generated in the CdS buffer layer and the corresponding CB is far from the electron quasi-Fermi level. On the contrary for high energy photons (400 nm) or under AM1.5 illumination, the secondary barrier is lowered at the CIGS/CdS interface as well as at CdS/ZnO interface. The barrier height reduction between ZnO window layer and CdS buffer layer results in cross-over of dark J–V (or low energy J–V) and AM1.5 J–V curves. This implies that higher voltage is required under dark conditions to maintain the same amount of current as that of AM1.5. A typical kinked J–V curve is seen for red light illumination. At smaller bias (<0.3 V), the 600 nm J–V curve is well-behaved and the current collection is proportional to AM1.5 illumination. But at higher bias (0.3 V $- V_{\text{OC}}$), the current collection is hindered resulting in red-kink. With further increase in bias ($>V_{\text{OC}}$), the J–V

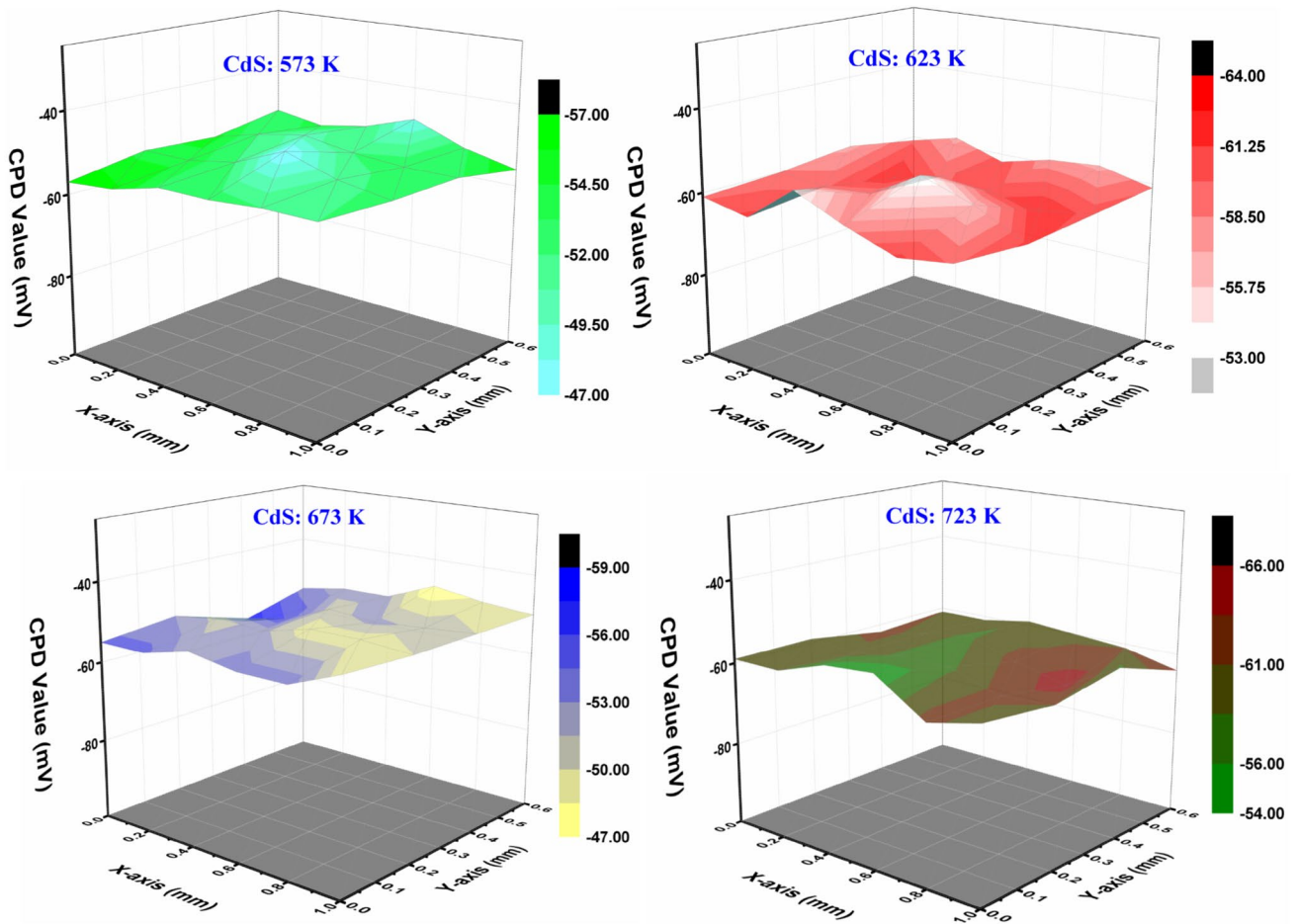


Fig. 9 (Colour online) CPD for CdS films annealed at different temperatures obtained from Kelvin probe measurement (scan area $1.0 \times 0.6 \text{ mm}^2$)

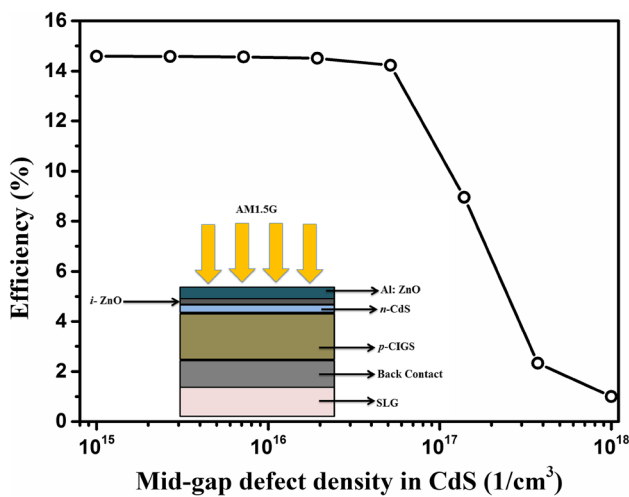


Fig. 10 (Colour online) Simulated CIGS/CdS solar cell efficiency as a function of CdS mid-gap acceptor density. The *inset* shows the proposed device structure

curve overlaps with that of dark. The photogenerated electrons in CIGS need to overcome the CIGS/CdS barrier thermionically to be collected as photocurrent. But, the energy barrier in the CIGS/CdS interface is more under 600 nm (red) illumination in the absence of photo-doping in CdS buffer layer. This results in a poor photocurrent collection and the J–V curve is kinked. This kind of photo-doping is suppressed when the mid-gap acceptor (mostly V_{Cd}^{2-}) concentration is low owing to lesser compensation of donors. We do not observe any kind of J–V distortions for CdS mid-gap acceptor density less than 10^{17} cm^{-3} (Fig. 11b). Poor compensation results in decreased barrier for all kinds of illumination and hence well behaved J–V characteristics. This leads to higher device efficiency. Similar kind of results have also been observed for kesterite solar cells [23, 49]. Moreover, less number of mid-gap defects means fewer recombination centers leading to higher conversion efficiency. In the present study for CdS thin films annealed at 723 K, the mid-gap acceptor (V_{Cd}^{2-}) density is minimized whereas the shallow donor type defects in the form

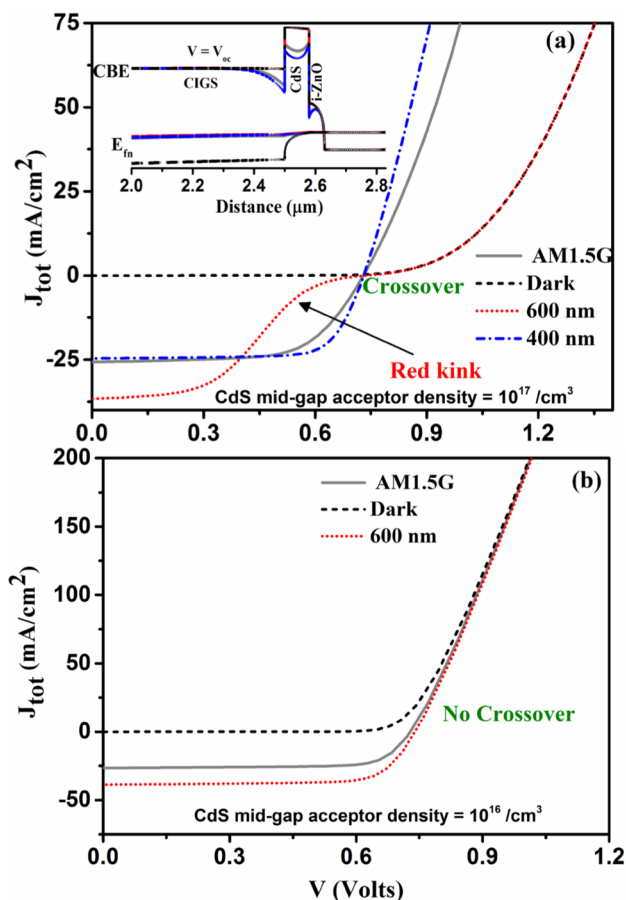


Fig. 11 (Colour online) **(a)** J–V characteristics for the model CIGS/CdS device under different kinds of illuminations (*inset* shows the corresponding energy band diagram) showing cross-over and red-kink for CdS mid-gap acceptor concentration of $10^{17}/\text{cm}^3$. **(b)** Well behaved J–V characteristics for CdS mid-gap acceptor concentration of $10^{16}/\text{cm}^3$

of cadmium interstitials and sulphur vacancies are present. These kind of poorly compensated CdS thin films are ideal to be used as buffer layers in CIGS based photovoltaic devices.

5 Conclusion

CdS thin films were prepared by sol–gel dip coating method on soda-lime glass substrates for potential use as buffer layers in chalcogenide solar cells. The films were annealed at different temperatures: 573, 623, 673 and 723 K for 1 h in air. XRD and Raman spectroscopy results show that the films crystallize in hexagonal wurtzite structure. The average grain size obtained from SEM is the highest (83.3 nm) for the films annealed at 723 K corresponding to improved carrier transport. The optical band gap value measured for CdS films annealed at 723 K is nearly the

same as that of bulk CdS (2.44 eV). Detailed analysis of the PL spectra reveals the defect structure in CdS thin films taking part in radiative transitions. Large number of surface states corresponding to the sulphur vacancies are observed at lower annealing temperatures. The lattice is healed at higher annealing temperatures and the interstitial atoms tend to occupy the vacant lattice sites. The films annealed at 573, 623 and 673 K are found to have NIR emissions corresponding to V_{Cd}^{2-} . These bivalent cadmium vacancies (V_{Cd}^{2-}) which are responsible for the photo-doping are minimized for the CdS films annealed at 723 K. Hence these films when used as buffer layers in chalcogenide solar cells can lead to an improvement in V_{OC} and FF without any J–V crossover. The strong exciton emission observed in these films further ensures better crystallinity. Low temperature PL confirms the presence of shallow level donors in these films together with emissions corresponding to free excitons and neutral-donor-bound excitons. The band gap at absolute zero temperature estimated from Varshni's relation is 2.565 eV. The surface work function for CdS films annealed at different temperatures is found to be ~ 4.7 eV. Numerical simulation studies for the model CIGS/CdS solar cell shows improved device performance together with well-behaved J–V characteristics for CdS films having mid-gap acceptor density less than 10^{17} cm^{-3} . However for practical devices, the issues related to the stability of the underneath absorber layer due to Cd diffusion and the role of oxygen at higher annealing temperatures need to be addressed. The effect of annealing at elevated temperatures in CIGS and $\text{Cu}_2\text{ZnSnSe}_4$ has been explained by Scragg et al. [50, 51]. They have shown that the vacuum annealing results in decomposition of metal sulphide/selenide and this can be avoided by annealing at high pressure. The other possible way to minimize the Cd diffusion into CIGS absorber layer is the optical annealing of CdS thin films from the top with a penetration depth of a few 10's of nm. Alternatively, the Cd diffusion can be suppressed by growing the CIGS photovoltaic device in the superstrate configuration with a relatively low temperature growth route for CIGS absorber layer.

Acknowledgements The authors gratefully acknowledge the financial support of New Indigo project [DST/IMRCD/New Indigo/PVMARS/2014/(G)] of the Department of Science and Technology, Government of India. The authors would also like to acknowledge Marc Burgelman, University of Gent, Belgium for providing the SCAPS solar cell simulator.

Appendix: Note on Kelvin probe technique to measure surface work function

The surface work function is defined as the energy required to remove an electron from the Fermi level to the vacuum

level. It is well known that the Fermi level depends upon the majority carrier density.

The basic operational principle of the Kelvin probe measurement is: when a (reference) metal tip is brought in close proximity of the surface of the test sample, a parallel plate capacitor is formed; the capacitance has the information of the surface work function of the sample. Since the capacitance or the surface charge measurement is extremely difficult, the reference electrode (or the Kelvin probe) is vibrated at a low frequency of 60–65 Hz, and an AC current is generated. Measurement of this current or equivalently the voltage is the Contact Potential Difference (CPD). The surface of the CdS sample is scanned over an area of 1.0 mm × 0.6 mm. The details of the circuitry and the measurement are described in the reference [25]. The relation between the CPD and the surface work function of the sample is given by Eq. 4.

$$e \cdot (\text{CPD}) = \Phi_{\text{ref}} - \Phi_{\text{sample}} \quad (4)$$

Here, Φ_{ref} and Φ_{sample} are the work functions of the reference metal tip and sample surface respectively.

References

- M.A. Green, K. Emery, Y. Hishikawa, W. Warta, E.D. Dunlop, Solar cell efficiency tables (version 48). *Prog. Photovolt: Res. Appl.* **24**, 905–913 (2016)
- K.L. Chopra, P.D. Paulson, V. Dutta, Thin-film solar cells: an overview. *Prog. Photovolt Res. Appl.* **12**, 69–92 (2004)
- A. Klein, Energy band alignment in chalcogenide thin film solar cells from photoelectron spectroscopy. *J. Phys. Condens. Matter.* **27**, 134201-1-134201-24 (2015)
- D.W. Niles, H. Hochst, Band offsets and interfacial properties of cubic CdS grown by molecular beam epitaxy on CdTe (110). *Phys. Rev. B* **41**, 12710–12719 (1990)
- B.S. Richards, K.R. McIntosh, Overcoming the poor short wavelength spectral response of CdS/CdTe photovoltaic modules via luminescence down-shifting: ray tracing simulations. *Prog. Photovolt Res. Appl.* **15**, 27–34 (2007)
- C.H. Chung, B. Bob, T.B. Song, Y. Yang, Current–voltage characteristics of fully solution processed high performance CuIn(S, Se)₂ solar cells: crossover and red kink. *Sol. Energ. Mat. Sol. Cells* **120**, 642–646 (2014)
- J.B. Varley, V. Lordi, Intermixing at the absorber-buffer layer interface in thin film solar cells: the electronic effects of point defects in Cu(In, Ga) (Se,S)₂ and Cu₂ZnSn(Se,S) 4 devices. *J. Appl. Phys.* **116**, 063505-1-063505-9 (2014)
- J.E. Moore, S. Dongaonkar, R.V.K. Chavali, M.A. Alam, M.S. Lundstrom, Correlation of built-in potential and I-V crossover in thin film solar cells. *IEEE J. Photovolt.* **4**, 1138–1148 (2014)
- R.H. Bube, *Photoconductivity of solids*. (John Wiley & Sons, London, 1960)
- K. Mochizuki, M. Satoh, K. Igaki, Orange luminescence in CdS. *Jpn. J. Appl. Phys.* **22**, 1414–1417 (1983)
- J.A. Hernandez, G.C. Puente, A.M. Acevedo, O.V. Galan, F.C. Gandarilla, J.V. Larramendi, A.E. Esquivel, H.H. Contreras, M.H. Garduno, A.A. Carbajal, M.C. Castaneda, G.A. Mejia, Photoluminescence and structural properties of cadmium sulphide thin films grown by different techniques. *Semicond. Sci. Technol.* **18**, 111–114 (2003)
- J.B. Varley, V. Lordi, Electrical properties of point defects in CdS and ZnS. *Appl. Phys. Lett.* **103**, 102103-1-102103-4 (2013)
- P. Elavarthi, A.A. Kumar, G. Murali, D.A. Reddy, K.R. Gunasekhar, Room temperature ferromagnetism and white light emissive CdS:Cr nanoparticles synthesized by chemical co-precipitated method. *J. Alloys Compd.* **656**, 510–517 (2016)
- A.E. Abken, D.P. Halliday, K. Durose, Photoluminescence study of polycrystalline photovoltaic CdS thin film layers grown by close-spaced sublimation and chemical bath deposition. *J. Appl. Phys.* **105**, 064515-1-064515-9 (2009)
- O. Vigil, I. Reich, M.G. Rocha, O.Z. Angel, Characterization of defect levels in chemically deposited CdS films in the cubic-hexagonal phase transition. *J. Vac. Sci. Technol. A* **15**, 2282–2286 (1997)
- S.T. Yam, R. Patino, A.I. Oliva, Chemical bath deposition of CdS films on different substrate orientations. *Curr. Appl. Phys.* **11**, 914–920 (2011)
- K.S. Balakrishnan, A.C. Rastogi, Structure and growth kinetics of electrodeposited CdS thin films for solar cell applications. *Sol. Energ. Mat. Sol. Cells* **20**, 417–434 (1990)
- A.A. Yadav, M.A. Barote, E.U. Masumdar, Studies on nanocrystalline cadmium sulphide (CdS) thin films deposited by spray pyrolysis. *Solid State Sci.* **12**, 1173–1177 (2010)
- A. A. Ziabari, F.E. Ghodsi, Growth characterization and studying of sol–gel derived CdS nanocrystalline thin films incorporated in polyethyleneglycol: Effects of post-heat treatment. *Sol. Energ. Mat. Sol. Cells* **105**, 249–262 (2012)
- M. Tomakin, M. Altunbas, E. Bacaksiz, S. Celik, Current transport mechanism in CdS thin films prepared by vacuum evaporation method at substrate temperatures below room temperature. *Thin Solid Films* **520**, 2532–2536 (2012)
- C.T. Tsai, D.S. Chuu, G.L. Chen, S.L. Yang, Studies of grain size effects in rf sputtered CdS thin films. *J. Appl. Phys.* **79**, 9105–9109 (1996)
- S. Keitoku, H. Ezumi, H. Osono, M. Ohta, Preparation of p-type CdS thin film by laser ablation. *Jpn. J. Appl. Phys.* **34**, L138–L140 (1995)
- M. Neuschitzer, Y. Sanchez, S.L. Marino, H. Xie, A. Fairbrother, M. Placidi, S. Haass, V.I. Roca, A.P. Rodriguez, E. Saucedo, Optimization of CdS buffer layer for high-performance Cu₂ZnSnSe₄ solar cells and the effects of light soaking: elimination of crossover and red kink. *Prog. Photovolt: Res. Appl.* **23**, 1660–1667 (2015)
- A.E. Danks, S.R. Hall, Z. Schnepf, The evolution of ‘sol–gel’ chemistry as a technique for material synthesis. *Mater. Horiz.* **3**, 91–112 (2016)
- A. Subrahmanyam, C. Suresh Kumar, *Kelvin probe for surface engineering*. (CRC Press, Florida, 2009)
- M. Burgelman, P. Nollet, S. Degraeve, Modelling polycrystalline semiconductor solar cells. *Thin Solid Films* **361–362**, 527–532 (2000)
- M. Burgelman, K. Decock, S. Khelifi, A. Abbas, Advanced electrical simulation of thin film solar cells. *Thin Solid Films* **535**, 296–301 (2013)
- P.K. Nair, O.G. Daza, A.A.C. Readigos, J. Campos, M.T.S. Nair, Formation of conductive CdO layer on CdS thin films during air heating. *Semicond. Sci. Technol.* **16**, 651–656 (2001)
- J. Chu, Z. Jin, S. Cai, J. Yang, Z. Hong, An in-situ chemical reaction deposition of nanosized wurtzite CdS thin films. *Thin Solid Films* **520**, 1826–1831 (2012)
- Y.N. Xu, W.Y. Ching, Electronic, optical and structural properties of some wurtzite crystals. *Phys. Rev. B* **48**, 4335–4351 (1993)

31. M. Gilic, J. Trajic, N. Romcevic, M. Romcevic, D.V. Timotijevic, G. Stanisic, Y.S. Yahia, Optical properties of CdS thin films. *Opt. Mater.* **35**, 1112–1117 (2013)
32. N. Maticiu, M. Kuk, N. Spalatu, T. Potlog, M. Krunks, V. Valdna, J. Hiie, Comparative study of CdS films annealed in neutral, oxidizing and reducing atmospheres. *Energy Procedia* **44**, 77–84 (2014)
33. F. Lisco, A. Abbas, B. Maniscalco, P.M. Kaminski, M. Losurdo, K. Bass, G. Claudio, J.M. Walls, Pinhole free thin film CdS deposited by chemical bath using a substrate reactive plasma treatment. *J. Renew. Sustainable. Energy* **6**, 011202-1-011202-9 (2014)
34. F. Boakye, D. Nusenu, The energy band gap of cadmium sulphide. *Solid State Commun.* **102**, 323–326 (1997)
35. R.D.L. Kristensen, S.N. Sahu, H. Haneman, Flash evaporation of CuInSe₂ films. *Sol. Energy Mater.* **17**, 329–345 (1988)
36. J.I. Pankove, *Optical Processes in Semiconductors*, (Dover, New York, 1971)
37. B. Ullrich, D.M. Bagnall, H. Sakai, Y. Segawa, Photoluminescence and lasing of thin CdS films on glass formed by pulsed-laser-deposition. *J. Lumin.* **87–89**, 1162–1164 (2000)
38. P. Kumar, N. Saxena, R. Chandra, K. Gao, S. Zhou, A. Agarwal, F. Singh, V. Gupta, D. Kanjilal, SHI induced enhancement in green emission from nanocrystalline CdS thin films for photonic applications. *J. Lumin.* **147**, 184–189 (2014)
39. P.Y. Yu, Enhancement of donor electronic Raman scattering in CdS. *Phys. Rev. B* **20**, 5286–5291 (1979)
40. P.K. Narayanam, P. Soni, P. Mohanta, R.S. Srinivasa, S.S. Talwar, S.S. Major, Effect of heat treatment on the photoluminescence of CdS nanocrystallites in cadmium rich organic Lngmuir Blodgett matrix. *Mater. Chem. Phys.* **139**, 196–209 (2013)
41. N. Susa, H. Watanabe, M. Wada, Effects of annealing in Cd and S vapor on photoelectric properties of CdS single crystals. *Jpn. J. Appl. Phys.* **15**, 2365–2370 (1976)
42. S. Achour, G.H. Talat, Effect of thermal annealing on the cathodoluminescence of evaporated CdS films. *Thin Solid Films* **144**, 1–6 (1986)
43. F. Gemain, I.C. Robin, S. Renet, S. Bernardi, Photoluminescence studies of CdS layers for solar cells. *Phys. Stat. Solidi. C* **9**, 1740–1743 (2012)
44. B. Gil, *Physics of wurtzite nitrides and oxides: passport to devices* (Springer, 2014)
45. S. Kijima, T. Nakada, High-temperature degradation mechanism of Cu(In,Ga)Se₂-based thin film solar cells. *Appl. Phys. Express* **1**, 075002-1-075002-3 (2008)
46. P. Atkins, *Physical Chemistry*, 5th Edition Oxford University Press, Oxford (1994)
47. F. Goto, K. Shirai, M. Ichimura, Defect reduction in electrochemically deposited CdS thin films by annealing in O₂. *Sol. Energ. Mat. Sol. Cells* **50**, 147–153 (1998)
48. Y.P. Varshni, Temperature dependence of the energy gap in semiconductors. *Physica* **34**, 149–154 (1967)
49. S.R. Meher, L. Balakrishnan, Z.C. Alex, Analysis of Cu₂ZnSnS₄/CdS based photovoltaic cell: a numerical simulation approach. *Superlattices Microstruct.* **100**, 703–722 (2016)
50. J.J. Scragg, P.J. Dale, D. Colombara, L.M. Peter, Thermodynamic aspects of the synthesis of thin-film materials for solar cells. *Chem. Phys. Chem.* **13**, 3035–3046 (2012)
51. J.J. Scragg, T. Ericson, T. Kubart, M. Edoff, C. Platzer-Björkman, Chemical insights into the instability of Cu₂ZnSnS₄ films during annealing. *Chem. Mater.* **23**, 4625–4633 (2011)